Heteroclinic Bifurcations Reveal Virtual Inertia–Damping Limits for Grid Stability

F. Bizzarri *, A.M. Brambilla*, D. del Giudice*, F. Dercole*, D. Linaro*
* Department of Electronics, Information Technology and Bioengineering, Politecnico di Milano, Milan, Italy.
Email: {federico.bizzarri, angelo.brambilla, davide.delgiudice, fabio.dercole, daniele.linaro}@polimi.it

***Abstract*—Modern electrical grids are witnessing an increasing share of inverter-based resources (IBRs) at generation and load side, while conventional generators and loads are being displaced. The resulting reduction in inertia and load damping exacerbates stability issues, particularly frequency and synchronization stability. To address this issue, the concept of virtual inertia and load damping has emerged, provided by the IBR control logic. This raises the question of how much intervention from IBRs is actually necessary, and if a too high contribution may yield adverse effects. We consider an aggregated model of a power-grid area, compact enough to be fully analyzed through the tools of nonlinear dynamics, to identify the key parameters influencing frequency and synchronization stability. We derive an operational expression showing that the ratio of grid area damping to inertia is of paramount importance rather than their individual values. These results are validated by simulating a well known benchmark electrical grid in different scenarios.**

***Index Terms*—Inertia, load damping, inverter based resources, frequency stability, dynamical systems, bifurcation analysis**

I. Introduction

The green transition is accelerating the integration of renewable energy sources (RESs), through converters that are displacing conventional power plants. This is causing the reduction of *inertia*, till nowadays provided by rotating masses of synchronous generators (SGs) [1]. Inertia is a key parameter of the rotor swing equation, which links power exchange to grid frequency. Its reduction weakens the system's ability to maintain rotor-angle and frequency stability (i.e., synchronism) after power imbalances [2]. Loss of synchronism is the most dangerous operating mode [3] and can trigger severe events, such as the recent Spanish blackout. Moreover, the increasing penetration of power-electronic converters, even on the load side, affects another parameter typically embedded in the swing equation: the *load damping*. It represents the effect of loads whose power consumption varies with the frequency of the AC power supply. To address the reducing trend in these quantities, the concept of virtual inertia and damping has emerged. In fact, to obtain additional inertia and damping, the control logic of converters interfacing RES-fuelled generators and loads (hereafter referred to as IBRs) is modified to emulate the electromechanical behaviour of synchronous generators and frequency-dependent loads [4]–[6].

Here, we address a key question: how much virtual inertia and load damping should be added to the power grid via IBRs? Can there be too much of a good thing? We show that, in a compact aggregated model of a power-grid area, the existence of a critical transition (a heteroclinic bifurcation) in the space of the model parameters provides a quantitative measure of the optimal ratio between inertia and load damping to guarantee synchronization stability. We validate our results by means of numerical simulations: in particular, we show stability results of a version of the IEEE 13-node test feeder [7] modified with the addition of IBRs fuelled by RESs and connected to a simplified model of a transmission system undergoing a large power imbalance.

The work of F. Bizzarri was partially supported by Italian MUR under the grant PRIN 2022 DCNanoSyn, CUP D53D23001500006, project code 2022SPFP9R.

II. The aggregated model of the power-grid area

We consider the power-grid area $\mathcal{A}$, schematically represented in Fig. 1. We assume that all SGs outside $\mathcal{A}$ can be grouped in an equivalent one and that their total inertia is sufficiently large to represent the equivalent generator as an infinite bus at voltage $v_{\text{bus}0} = \rho_0 e^{\mathbb{i}\theta_0}$ ($\mathbb{i} = \sqrt{-1}$). Similarly, all SGs in $\mathcal{A}$ are assumed coherent (i.e., they react analogously to power imbalances). Hence, they can be grouped in an equivalent machine G_{eq} with voltage angle θ_1, that we model by the classical swing equation

$$\begin{cases} \dot{\theta} = \Omega_b \Delta\omega \\ 2HS_b\Delta\dot{\omega} = P_m - P_e - DS_b\Delta\omega \end{cases}, \tag{1}$$

where $\theta = \theta_1 - \theta_0$ is the angle imbalance w.r.t. BUS0 and $\Delta\omega = \omega - 1$ [pu] is the deviation of the rotor angular speed ω [pu] from the nominal angular frequency $\Omega_b\,[\mathrm{rad\,s^{-1}}]$. In Eq. (1), S_b [pu] is the nominal capacity of the synchronous generator w.r.t. the $S_0\,[\mathrm{MVA}]$ reference, P_m [pu] is the mechanical power, P_e [pu] is the active power of the synchronous generator (positive generated),[1] H [s] is the equivalent inertia, and D is the equivalent load damping. All loads in $\mathcal{A}$ are grouped in the equivalent load L, absorbing the active power P_L/S_0 [pu] at power flow (PF). G_{eq} and L are connected to BUS1 at $v_{\text{bus}1} = \rho_1 e^{\mathbb{i}\theta_1}$ [V].

The lines connecting $\mathcal{A}$ to the neighbouring areas can be replaced by a single equivalent one with the same overall area short circuit ratio (SCR). Based on Fig. 1, $\text{SCR} = \rho_1^2/(S_b S_0 |Z|)$, where $|Z| = \sqrt{R^2 + X^2}$. By defining $G = R/|Z|^2$, the active power [pu] flowing through the line from BUS1 to BUS0 is

$$P_{\text{TIE}} = \frac{\rho_1^2 G}{S_0} + S_b \text{SCR} \frac{\rho_0}{\rho_1} \sin\left(\theta - \arctan\frac{R}{X}\right), \tag{2}$$

[1] P_m and P_e are expressed in pu w.r.t. S_0 [MVA].

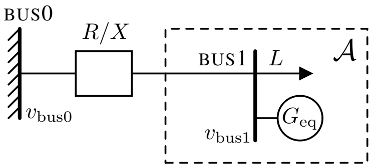

Fig. 1. The schematic of the simple test system. R and X are the resistance and the reactance of the line connecting BUS1 to the infinite bus BUS0.

so that, in (1), we can substitute $P_e = {}^{P_L}/_{S_0} + P_{\text{TIE}}$.

By introducing the normalization parameters

$$\epsilon = \frac{D}{2H}\,,\ \alpha = \text{SCR}\frac{\rho_0}{\rho_1}\frac{\Omega_b}{2H}\,,\ \mu = \frac{\Omega_b}{2H}\frac{P_m S_0 - P_L - \rho_1^2 G}{S_b S_0}\,,$$

and the normalized state variables

$$x = \theta - \arctan\left({}^{R}/_{X}\right) + \arcsin\left({}^{\mu}/_{\alpha}\right) \text{ and } y = \dot{x} = \Omega_b \Delta\omega\,, \tag{3}$$

the dynamical system under study can be recast as

$$\ddot{x} + \epsilon\dot{x} + \alpha\sin\left(x - \arcsin{}^{\mu}/_{\alpha}\right) = \mu\,, \tag{4}$$

which, interestingly, appeared in other research field [8], [9].

III. Bifurcation analysis

The equilibrium points of (4), for ${}^{\mu}/_{\alpha} \in (-1, 1)$ are

$$E_{\text{u}_k} = [\pi + 2\pi k, 0]^{\text{T}} \triangleq [x_{\text{u}_k}, 0]^{\text{T}}$$
$$E_{\text{s}_k} = \left[2\left(\arcsin{}^{\mu}/_{\alpha} + \pi k\right), 0\right]^{\text{T}} \triangleq [x_{\text{s}_k}, 0]^{\text{T}}\,,\ k \in \mathbb{Z}\,.$$

The eigenvalues of the Jacobian matrix of (4) at $E_{\{\text{u,s}\}_k}$ are

$$\lambda_{\text{u}}^{\pm} = -\frac{\epsilon \pm \sqrt{\epsilon^2 + \Xi(\mu,\alpha)}}{2},\ \lambda_{\text{s}}^{\pm} = -\frac{\epsilon \pm \sqrt{\epsilon^2 - \Xi(\mu,\alpha)}}{2}\,,$$

where $\Xi(\mu, \alpha) = 4\alpha\sqrt{1 - ({}^{\mu}/_{\alpha})^2}$. E_{u_k} are hyperbolic saddle points for any choice of the parameter values, whereas the curve $\chi(\mu, \epsilon, \alpha) \triangleq \epsilon^2 - \Xi(\mu, \alpha)$ (black in Fig. 2) separates the parameter space into the regions where E_{s_k} are either stable nodes ($\chi(\mu, \epsilon, \alpha) > 0$, above the black curve) or stable foci ($\chi(\mu, \epsilon, \alpha) < 0$, below the black curve). The vertical lines ${}^{\mu}/_{\alpha} = \pm 1$ represent saddle-node bifurcations where each pair of equilibria E_{u_k} and E_{s_k} collides and disappears, viz. (4) admits no equilibria for ${}^{\mu}/_{\alpha} \notin (-1, 1)$.

In the limit case where $\epsilon = 0$ (i.e., $D = 0$, no load damping and droop in the area), E_{s_k} becomes non-hyperbolic, as $\lambda_{\text{s}}^{\pm}$ are purely imaginary and (4) reduces to a Hamiltonian system with first integral [10]

$$\mathcal{H}(x, y) = \frac{y^2}{2} - \mu x - \alpha\cos\left(x - \arcsin{}^{\mu}/_{\alpha}\right).$$

The function $V(x) \triangleq -\mu x - \alpha\cos(x - \arcsin{}^{\mu}/_{\alpha})$ plays the role of a potential function and the equilibria E_{s_k} and E_{u_k} are local extrema of $V(x)$, as shown in the upper panel of Fig. 3).

The global structure of the solution curves of (4) for $\epsilon = 0$, are given by $\mathcal{H}(x, y) = c$ (where c is a real constant), or $y = \pm\sqrt{2(c - V(x))}$, which turns out to be symmetric under reflection about the x-axis. A major consequence of this is that, if there are two saddle points with the same potential level with no higher (or equal) maximum between them, they must be connected by heteroclinic orbits [10]. This happens for $\mu = 0$, since $V(x_{\text{u}_k}) = V(x_{\text{u}_{k+1}}) > V(x_{\text{s}_k})$, for any $k \in \mathbb{Z}$ (see the gray curve in the upper panel of Fig. 3). In this case, there is a double heteroclinic connection between each pair of contiguous E_{u_k} (see the lower panel in Fig. 3).

For $\epsilon = 0$ and $\mu \neq 0$, the system exhibits homoclinic connections to the E_{u_k} saddles (along the $\kappa^{\pm}$ curve) in Fig. 2), as it is shown in the lower panel of Fig. 3. The existence of these orbits can be justified by observing, in the upper panel of Fig. 3, the presence of x values, say x_k^- between each pair of saddles $\{E_{\text{u}_k}, E_{\text{u}_{k+1}}\}$ for $\mu < 0$ and x_k^+ between saddles $\{E_{\text{u}_{k-1}}, E_{\text{u}_k}\}$ for $\mu > 0$, where $V(x_k^{\pm}) = V(x_{\text{u}_k})$. Two examples are reported in the upper panel of Fig. 3 (see black diamonds): $x_0^- \in (x_{\text{u}_0} \equiv \pi, x_{\text{u}_1} \equiv 3\pi)$ where $V(x_0^-) = V(x_{\text{u}_0}) \equiv V(\pi)$ and $x_0^+ \in (x_{\text{u}_{-1}} \equiv -\pi, x_{\text{u}_0} \equiv \pi)$ where $V(x_0^+) = V(x_{\text{u}_0}) \equiv V(\pi)$. Furthermore, the system admits infinite non-attractive closed orbits corresponding to the level curves $\mathcal{H}(x, y) = c$ for constant values of $c \in (V(x_{\text{s}_k})), V(x_k^{\pm})]$. These closed orbits lie within areas of the state-plane delimited by the aforementioned homoclinic connections, as shown by the simulated orbits reported in Fig. 4 (upper panel, red orbits). Outside homoclinic connections, orbits are unbounded, with the angle unbalance x (a shifted version of θ, see (3)) running to $+\infty$ with ever increasing, on average, speed y (proportional to $\Delta\omega$).

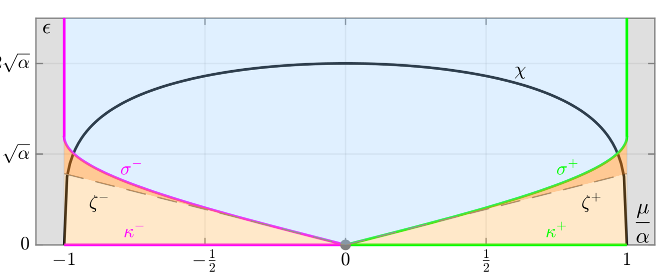

Fig. 2. Bifurcation diagram (obtained for $\alpha = 4$). Curves: χ (black) separates stable nodes E_{s_k} (above) from stable foci E_{s_k} (below); $\sigma^{\pm}$ (green and purple) are heteroclinic bifurcations; $\zeta^{\pm}$ (dashed) are their first order approximation at $(\mu, \epsilon) = (0, 0)$; $\kappa^{\pm}$ (green and purple at $\mu = 0$) are homoclinic bifurcations.

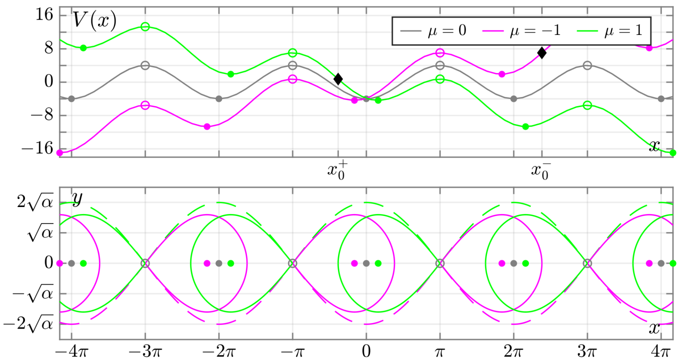

Fig. 3. The case $\epsilon = 0$ ($\alpha = 4$). Upper panel: solid and empty circles are local minima and maxima of the $V(x)$ potential function assumed at x_{s_k} and x_{u_k}, respectively. Black diamonds correspond to $x_0^{\pm}$ (see text). Lower panel: heteroclinic (dashed) and homoclinic (solid) connections to the E_{u_k} saddle points. Solid circles represent E_{s_k}.

For $\epsilon > 0$, the solutions of (4) approach, at $\epsilon-$exponential rate $S = \{(x, y) : \mu - \alpha \leq \epsilon y \leq \mu + \alpha\}$, which is an invariant strip. According to [8], [9], it is possible to locate in the (μ, ϵ, α) parameters space the heteroclinic bifurcation manifolds $\sigma^{\pm}(\mu, \epsilon, \alpha) = 0$. A projection of these manifolds (originated at $(\mu, \epsilon) = (0, 0)$ at $\alpha = 4$) on the (μ, ϵ) plane, is shown in Fig. 2. These curves have been numerically obtained with Matlab's [11] continuation toolbox MATCONT [12]–[14]. For parameter values belonging to σ^{+}, heteroclinic connections similar to the dashed green ones in the lower panel of Fig. 3 are solutions of (4). *Mutatis mutandis* the same holds for σ^{-} and the dashed magenta heteroclinic connections. The saddle-node vertical curves $\mu = \pm\alpha$ are asymptotes for $\sigma^{\pm}$. It is worth mentioning that, similarly to what is done in [9], it is possible to derive the following first order approximation at $(\mu, \epsilon) = (0, 0)$, for $\alpha > 0$, of $\sigma^{\pm}$

$$\sigma^{\pm}(\mu, \epsilon, \alpha) \simeq \zeta^{\pm}(\mu, \epsilon, \alpha) \triangleq 4\epsilon\sqrt{\alpha} - |\mu| \,. \tag{5}$$

The $\zeta^{\pm}(\mu, \epsilon, 4) = 0$ curves are shown in Fig. 2 (dashed gray).

For parameter values between $\sigma^{\pm}$ and $\kappa^{\pm}$ (see light and dark orange areas in Fig. 2), we observe, in accordance with [8], [15], the coexistence of the stable equilibria E_{s_k} with a stable *running periodic solution* [15], [16] (see the attractive green orbit in Fig. 4, lower panel). It is a periodic solution because x is 2π-periodic variable (a shifted version of the angle unbalance θ, see (3)) running to $+\infty$ with periodic speed y (proportional to $\Delta\omega$). [2] The basin of attraction of the periodic solution is highlighted by the black orbits in the simulations reported in Fig. 4 (lower panel), whereas the red orbits are within the basins of attraction of the stable equilibria E_{s_k}.

IV. The operative expression

From the power system modeling point of view, the bifurcation diagram reported in Fig. 2 highlights the light blue colored working region in the parameters space in which it is desirable to operate. First of all, we must have $|\mu/\alpha| \leq 1$ since otherwise E_{s_k} does not exist. By considering the expressions of μ and α and by deriving through (2) that

$$P_m S_0 - P_L - \rho_1^2 G = S_0 S_b \mathrm{SCR} \frac{\rho_0}{\rho_1} \sin\left(\theta - \arctan\frac{R}{X}\right),$$

this inequality translates in $|\sin(\theta - \arctan(R/X))| \leq 1$, which is always true. It is always satisfied, if the grid admits an operating point, i.e., if it behaves *properly* by being able to exchange the desired power through the line. Importantly, to avoid the coexistence of stationary solutions with undesired oscillations, thus avoiding synchronization stability issues, the system must operate above the $\sigma^{\pm}$ heteroclinic bifurcation curves. This can be obtained by increasing the parameter $\epsilon = D/2H$, that is, by regulating the *ratio* between damping and inertia and not by simply acting on the inertia of an area, which is usually suggested in the literature to tackle frequency stability issues in IBR-dominated grids. A possible and simple design rule is provided by (5), rewritten in terms of the

[2] It is a standard limit cycle in the cartesian coordinates $(\sin x, \cos x, y)$.

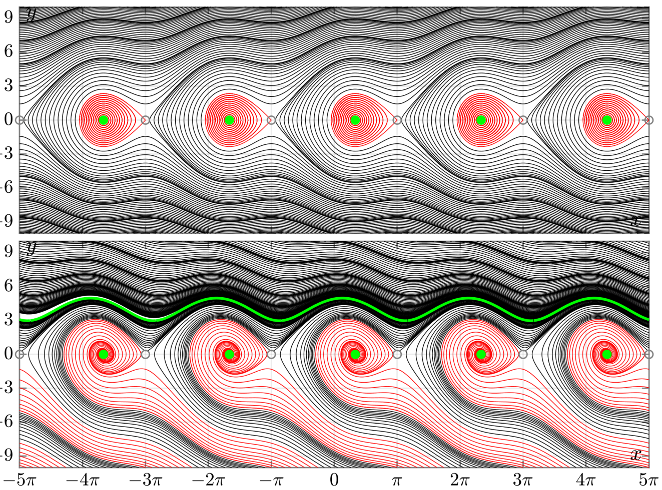

Fig. 4. Simulated orbits for $\epsilon = 0$ (upper panel) and for $\epsilon = 0.5$ (lower panel). Other parameters: $\alpha = 4$, $\mu = 2$.

original system parameters and solved w.r.t. D[3]. Neglecting the resistance R (i.e., $G = 0$) and assuming the ρ_1 modulus of the voltage at BUS1 is kept equal (very close) to that of the infinite bus,[4] some simple algebra yields

$$D = \frac{1}{2}\sqrt{\frac{\Omega_b H}{2\mathrm{SCR}}} \left|\frac{P_m S_0 - P_L}{S_b S_0}\right| \triangleq D^0_{\min}\,, \tag{6}$$

which is the minimum value of D necessary for the system to operate above the heteroclinic bifurcation curves for a given set of other system parameters, H included.

V. Numerical results

The proposed model was tested on the modified version of the IEEE 13-node test feeder in Fig. 5 [7]. The benchmark, working at $\Omega_b = 2\pi\,60\,\mathrm{rad\,s^{-1}}$, is of small-scale and characterized by relatively highly unbalanced loads, a single voltage regulator at the substation, overhead and underground lines, shunt capacitors, and an in-line transformer. With respect to its original version, this feeder version has additional elements (in violet). Among these, there is a $4\,\mathrm{pu}$ SG (we assume $S_0 = 100\,\mathrm{MVA}$ thus its capacity is $400\,\mathrm{MVA}$). Its inertia and damping coefficient are $5\,\mathrm{s}$ and 1, respectively. The SG is equipped with a turbine governor having a $5\,\mathrm{s}$ time constant and a droop coefficient equal to 50. The SG is connected to node 632 through a transmission line ($R = 0$ and $X = 6.302\,\Omega$) and a transformer added to step down the voltage from $15\,\mathrm{kV}$ at the generator output to the $4.16\,\mathrm{kV}$ of the feeder. The L_1 load is resistive and absorbs $1.04\,\mathrm{pu}$ per phase. Including SG and L_1 in the grid makes it more realistic than an infinite bus, and we will show that (6) remains a good operational bound to ensure synchronization stability.

We connected IBRs of $S_b = 0.1\,\mathrm{pu}$ nominal capacity at nodes 680, 675, and 633. These IBRs are of grid-forming (GFM) type, they provide both virtual inertia and load damping

[3] As it can be noticed in Fig. 2, the small dark orange regions are not excluded if $\zeta^{\pm}$ are taken as a boundary instead of $\sigma^{\pm}$. It is a price to be paid if one wants to exploit the simple expression in (5).

[4] This means we assume that voltage regulators in the area work properly.

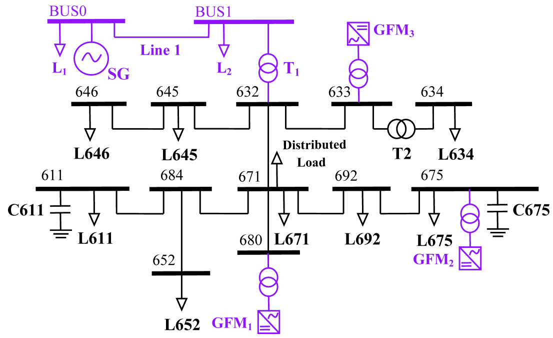

Fig. 5. The modified IEEE 13-node feeder: extra elements are in violet.

with a specific control logic [17]: their values are initially assumed to be $H_{\mathrm{GFM}}=3\,\mathrm{s}$ and $D_{\mathrm{GFM}}=2.25$, respectively, for all IBRs[5]. The active power set-point of GFM_1 is $0.03\,\mathrm{pu}$ (i.e., $0.03 S_0/S_b = 3\,\mathrm{MW}$), whereas that of GFM_2 and GFM_3 is $0.015\,\mathrm{pu}$. The reactive power set-point of all of them is null. In this case study, the area $\mathcal{A}$ in Fig. 1 includes the loads of the feeder that, summed up to L_2, yield L. The active power absorbed by the feeder loads is close to $0.03\,\mathrm{pu}$ (i.e., $3\,\mathrm{MW}$). The equivalent G_{eq} generator represents the combined action at BUS1 (area boundary bus) of the three IBRs. The parameters of G_{eq} are assumed to be $H=3H_{\mathrm{GFM}}$, $D=3D_{\mathrm{GFM}}$, and $P_m=0.06$ (i.e., $0.06 S_0/S_b = 6\,\mathrm{MW}$). Since we assume $\rho_0=\rho_1=15\,\mathrm{kV}$, we obtain $\mathrm{SCR}=4.16$.

L_2 is used to simulate a load change in $\mathcal{A}$: in particular, when its P_{L_2} active power is zero, the one generated by the three GFM IBRs is enough to supply the feeder, and almost $0.03\,\mathrm{pu}$ (i.e., $3\,\mathrm{MW}$) are exported through the line as a contribution to supply L_1. For $t<1\,\mathrm{s}$, the system works at steady state, as shown by the curves in Fig. 6, which depict the (virtual) angular frequency of the three IBRs. Black, magenta, and green curves refer to the three case studies described in the following. At $t=1\,\mathrm{s}$, P_{L_2} is step-changed to $0.26\,\mathrm{pu}$ (i.e., $26\,\mathrm{MW}$). So doing, the line is used to let the SG support the three GFM IBRs in supplying the $\mathcal{A}$ area.

A. Case I ($H_{\mathrm{GFM}}=3\,\mathrm{s}$ and $D_{\mathrm{GFM}}=2.25$)

In this case, for $t<1\,\mathrm{s}$, $D^0_{\min}\approx 1.03 < D = 3D_{\mathrm{GFM}}$. According to Sec. II, the simplified model corresponding to Fig. 5 exhibits a stable equilibrium point only. Being $D > D^0_{\min}$ and having in mind (6) and (5), the system is working above the $\zeta^{\pm}$ curves in Fig. 2. At $t>1\,\mathrm{s}$, because of the step-change of P_{L_2}, $D^0_{\min}\approx 7.72 > D$. The equilibrium point is no longer the only stable attractor and, as indicated by the black curves in Fig. 6, the dynamics is attracted by a running periodic solution. This is confirmed by the inset, where the black curves are shown in the last $50\,\mathrm{ms}$ of the simulation. The fundamental frequency of these curves does not correspond to $2\,\Omega_b$, as one could expect, being the feeder an unbalanced three-phase system[6].

[5]We assume that their internal controllers have infinite bandwidth compared to the relatively slower process of power system frequency regulation.

[6]A running periodic solution (e.g., the green trajectory in Fig. 4) can remain within the admissible angular-speed bounds, yielding persistent but non-disruptive oscillations (a synchronization-stability issue); in Fig. 6, instead, the average value falls far outside the limits, resulting in a catastrophic frequency-stability outcome.

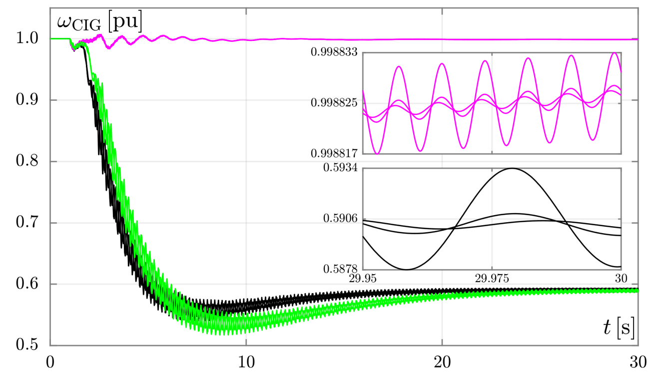

Fig. 6. Virtual angular speed of the IBRs. Black, green and magenta curves correspond to Case I, II, and III, respectively.

B. Case II ($H_{\mathrm{GFM}}=4\,\mathrm{s}$ and $D_{\mathrm{GFM}}=2.25$)

To mitigate the dangerous behavior described above, it is considered *a good practice to increase the inertia of the system* by acting on the contribution offered by the IBRs to fast frequency response. In this case, for $t<1\,\mathrm{s}$, $D^0_{\min}\approx 1.19 < D = 3D_{\mathrm{GFM}}$ but, for $t>1\,\mathrm{s}$, the situation is worse than in the previous scenario. Indeed, because of the step-change of P_{L_2}, $D^0_{\min}\approx 8.91 > D$. The running periodic solution is once more present (see the green curves in Fig. 2). Thus, in contrast to conventional belief, in this case increasing the inertia causes the grid to operate in a worse condition than the one characterized by lower inertia. Beware, however, that this does not mean that decreasing H is a viable solution to achieve stability. Indeed, H still has to be regulated to limit the rate of change of frequency (ROCOF) after power imbalances.

C. Case III ($H_{\mathrm{GFM}}=3\,\mathrm{s}$ and $D_{\mathrm{GFM}}=4.5$)

This problem can be mitigated by increasing not H (which inherently reduces ϵ) but D. For $t<1\,\mathrm{s}$, $D^0_{\min}\approx 1.03 < D = 3D_{\mathrm{GFM}}$ but now this is true also for $t>1\,\mathrm{s}$ since $D^0_{\min}\approx 7.72 < D = 3D_{\mathrm{GFM}} = 13.5$. The running periodic solution no longer coexists with the stable equilibrium point and thus the dynamics of the system is stable. The evolution of the system is given by the magenta curves in Fig. 2, shown in the last $50\,\mathrm{ms}$ of the simulation in the inset. The fundamental frequency of these curves corresponds to $2\,\Omega_b$, as expected, being the feeder an unbalanced three-phase system.

VI. Concluding Remarks

This paper employs a reduced but still significant and accurate model of a grid area to show that frequency/synchronization stability against large power imbalances occurring in a grid area can be ensured by acting not exclusively on the inertia constant H but also on the load damping coefficient D. Thus, the ratio H/D is one of the key parameters of an area that must be monitored during the green transition. We gave an operative expression to check if an area is working with a proper H/D ratio ensuring synchronization stability. Simulation results proved the effectiveness of the proposed approach and operative expression.

References

[1] P. Kundur, N. Balu, and M. Lauby, *Power system stability and control*, ser. EPRI power system engineering series. McGraw-Hill, 1994.

[2] P. Makolo, R. Zamora, and T.-T. Lie, "The role of inertia for grid flexibility under high penetration of variable renewables - A review of challenges and solutions," *Renew. Sustain. Energy Rev.*, vol. 147, no. 111223, 2021.

[3] C. He, X. He, H. Geng, H. Sun, and S. Xu, "Transient stability of low-inertia power systems with inverter-based generation," *IEEE Transactions on Energy Conversion*, vol. 37, no. 4, pp. 2903–2912, 2022.

[4] H.-P. Beck and R. Hesse, "Virtual synchronous machine," in *2007 9th International Conference on Electrical Power Quality and Utilisation*, 2007, pp. 1–6.

[5] S. D'Arco and J. A. Suul, "Equivalence of Virtual Synchronous Machines and Frequency-Droops for Converter-Based MicroGrids," *IEEE Trans. Smart Grid*, vol. 5, no. 1, pp. 394–395, Jan. 2014.

[6] U. Tamrakar, D. Shrestha, M. Maharjan, B. P. Bhattarai, T. M. Hansen, and R. Tonkoski, "Virtual inertia: Current trends and future directions," *Applied sciences*, vol. 7, no. 7, p. 654, 2017.

[7] K. P. Schneider, B. A. Mather, B. C. Pal, C.-W. Ten, G. J. Shirek, H. Zhu, J. C. Fuller, J. L. R. Pereira, L. F. Ochoa, L. R. de Araujo, R. C. Dugan, S. Matthias, S. Paudyal, T. E. McDermott, and W. Kersting, "Analytic considerations and design basis for the IEEE distribution test feeders," *IEEE Trans. on Power Systems*, vol. 33, no. 3, pp. 3181–3188, 2018.

[8] M. Levi, F. C. Hoppensteadt, and W. L. Miranker, "Dynamics of the Josephson junction," *Quarterly of Applied Mathematics*, vol. 36, no. 2, pp. 167–198, 1978.

[9] P. Coullet, J. M. Gilli, M. Monticelli, and N. Vandenberghe, "A damped pendulum forced with a constant torque," *American Journal of Physics*, vol. 73, no. 12, pp. 1122–1128, 12 2005.

[10] J. Guckenheimer and P. Holmes, *Nonlinear oscillations, dynamical systems, and bifurcations of vector fields*. Berlin: Springer Verlag, 1983.

[11] T. M. Inc., "MATLAB version: 24.2.0.2806996 (R2024b)," The MathWorks Inc., Natick, Massachusetts, United States, Tech. Rep., 2024. [Online]. Available: https://www.mathworks.com

[12] A. Dhooge, W. Govaerts, and Y. A. Kuznetsov, "MATCONT: A MATLAB package for numerical bifurcation analysis of ODEs," *ACM Trans. Math. Softw.*, vol. 29, no. 2, p. 141–164, Jun. 2003.

[13] A. Dhooge, W. Govaerts, Y. A. Kuznetsov, H. G. Meijer, and B. Sautois, "New features of the software MatCont for bifurcation analysis of dynamical systems," *Mathematical and Computer Modelling of Dynamical Systems*, vol. 14, no. 2, pp. 147–175, 2008.

[14] V. De Witte, W. Govaerts, Y. A. Kuznetsov, and M. Friedman, "Interactive initialization and continuation of homoclinic and heteroclinic orbits in MATLAB," *ACM Trans. Math. Softw.*, vol. 38, no. 3, Apr. 2012.

[15] F. Tricomi, "Integrazione di un' equazione differenziale presentatasi in elettrotecnica," *Annali della Scuola Normale Superiore di Pisa - Scienze Fisiche e Matematiche*, vol. 2, pp. 1–20, 1933.

[16] F. Hoppensteadt, *Analysis and Simulation of Chaotic Systems*, ser. Applied Mathematical Sciences. Springer New York, 2000.

[17] A. M. Brambilla, D. d. Giudice, and F. Bizzarri, "Improved stability of a grid-following converter controller supplying virtual inertia and damping," *IEEE Transactions on Power Delivery*, vol. 40, no. 2, pp. 900–911, 2025.